Solution Synthesis of Ultrathin Single-Crystalline SnS Nanoribbons for Photodetectors *via* Phase Transition and Surface Processing

Zhengtao Deng,[†,§,*] Di Cao,[†,§] Jin He,[‡] Su Lin,[†] Stuart M. Lindsay,[†] and Yan Liu[†,*]

[†]The Biodesign Institute, and Department of Chemistry and Biochemistry, Arizona State University, Tempe, Arizona 85287, United States and [‡]Department of Physics, Florida International University, Miami, Florida 33199, United States. [§]These authors contributed equally to this work.

ABSTRACT We report the solution-phase synthesis and surface processing of ~2–5 μm long single-crystalline IV–VI tin(II) sulfide (SnS) ultrathin nanoribbons, with thicknesses down to 10 nm, and their use in single nanoribbon based photodetectors. The SnS nanoribbons grow *via* a metastable-to-stable phase transition from zinc blende (ZB) nanospheres to orthorhombic nanoribbons; dual-phase intermediate heterostructures with zinc blende nanosphere heads and orthorhombic nanoribbon tails were observed. Exchange of long, insulating organic oleylamine ligands by short, inorganic HS^- ligands converts the organic SnS nanoribbons into completely inorganic, hydrophilic structures. Field-effect transistor (FET) devices were made from single SnS nanoribbons, both before and after ligand exchange, which exhibit p-type semiconductor behavior. The SnS single nanoribbon based photodetector devices showed highly sensitive and rapid photocurrent responses to illumination by blue, green, and red light. The switching behavior of photocurrent generation and annihilation is complete within approximately 1 ms and exhibits high photoconductivity gains (up to 2.3×10^4) and good stability. The ON/OFF ratio of the photodetector can be engineered to 80 (4 nA/50 pA) using a small drain current (10 mV) for the all inorganic SnS nanoribbons. This work paves the way for the colloidal growth of low-cost, environmentally benign, single-crystalline narrow band gap semiconductor nanostructures from abundant elements for applications in photodetectors and other nanoscale devices.

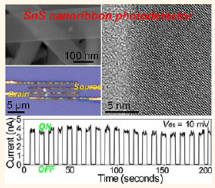

KEYWORDS: colloidal nanoribbons · phase transition · ligand exchange · field-effect transistors · photodetector · tin sulfide

Quasi-one-dimensional (quasi-1D) ribbon-like structures (nanoribbons) were found to have unusual electronic and thermal transport properties compared to one-dimensional nanowire and nanotube materials.[1−4] These fascinating materials exhibit novel physical properties owing to their unique geometries, with high aspect ratios and ultrathin thicknesses. They are the potential building blocks for a wide range of nanoscale electronics, optoelectronics, and sensing devices.[5−7] Among these, photodetectors are critical for applications as binary switches in imaging techniques and light-wave communications, as well as in future memory storage and optoelectronic circuits.[8−10]

Great efforts have been devoted to synthesize and characterize quasi-1D nanoribbons with various elemental compositions.[2,4,6,7,11−13] Parallel to the success with group IV (such as graphene[1,14]) and groups III–V (such as BN[3,4]) compounds, earth-abundant main-group IV–VI (IV = Ge, Sn, Pb; VI = S, Se, Te) semiconducting materials have also attracted significant attention, due to their narrow band gap and rich optical, electronic, and optoelectronic properties.[15,16] Among these, tin(II) sulfide (SnS) is a low-cost, earth-abundant (260 ppm sulfur, 2.2 ppm tin in the earth's crust, compared to 0.05 ppm selenium, 0.049 ppm indium, and 0.005 ppm tellurium), nontoxic, and heavy-metal-free (*i.e.*, free from Cd, Pb, and Hg) semiconductor material with narrow band gaps of 1.1 eV (indirect) and 1.3 eV (direct).[17−22] Avoiding the use of rare metals, such as indium, selenium, and tellurium, reduces the burden of demand in the future. Theoretical calculations indicate that SnS possesses all of the qualities required for efficient absorption of solar energy and is suitable for incorporation into clean energy conversion cells.[16,22−26] It also has other useful properties, such as photoconducting, photocatalytic, and Peltier effects, which make it a promising material for diverse applications in thermoelectric cooling, thermoelectric power generation, and near-infrared photoelectronics.[15,16,27−29]

SnS nanocrystals and microcrystals with either orthorhombic[17,18,30−32] or zinc blende (ZB)[30,33] phases have already been reported. Crystalline SnS wires of mixed micro- and

* Address correspondence to yan_liu@asu.edu, zhengtao.deng@asu.edu.

Received for review April 9, 2012 and accepted June 27, 2012.

Published online June 27, 2012
10.1021/nn302504p

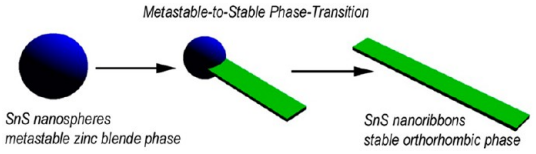

Scheme 1. Schematic illustration of the growth of a single-crystalline SnS nanoribbon *via* a metastable-to-stable phase transition process. The blue sphere represents the metastable zinc blende phase, while the green ribbon represents the stable orthorhombic phase.

nanometer scale features have been synthesized over tin metal foils using a surfactant-assisted approach.[34] In a recent study, 50 nm diameter SnS nanowires were synthesized by the pulsed electrochemical deposition method using porous anodized aluminum oxide templates.[35] However, synthesis of SnS nanostructures with well-defined crystallinity, size, and morphology as well as the investigation of their optical, electrical, and photoconductive properties remains a challenge. Here, we demonstrate the first colloidal synthesis of ultrathin, single-crystalline SnS nanoribbons with thicknesses down to 10 nm *via* a unique metastable-to-stable phase transition process. We also demonstrated that a simple inorganic ligand HS^- can be used to replace the original organic oleylamine ligand, imparting hydrophilicity to the structures. Field-effect transistor (FET) devices based on single SnS nanoribbons were fabricated and exhibited p-type behavior. Although inorganic chalcogenide ligands have led to record high electronic transport parameters in colloidal quantum dot arrays,[36] the report here is the first time that the electronic behaviors of single 1D or quasi-1D colloidal nanostructure based devices were investigated using such a technique. Furthermore, we studied the photoconductivity of a single SnS nanoribbon based photodetector. To the best of our knowledge, this is the first example of a single SnS nanostructure based photodetector.

RESULTS AND DISCUSSION

The synthetic scheme we employed for the synthesis of SnS nanoribbons is based on our previously reported phosphine-free colloidal method for synthesizing II–VI nanocrystals.[37] Experimental procedures are detailed in the materials and methods section. The resulting single-crystalline SnS nanoribbons are ~2–5 μm long and ~150–500 nm wide, with thicknesses of ~10 nm. Their formation occurs by a simple colloidal process, initiated by the injection of a sulfur-oleylamine precursor into a hot tin-oleylamine solution in the presence of hexamethyldisilazane (HMDS). During the synthesis, sequential aliquots of the reaction mixture were removed and purified to monitor the kinetics of nanoribbon formation. As shown in Scheme 1, single-crystalline SnS nanoribbons formed through a unique phase transition pathway from the metastable zinc blende phase to the stable orthorhombic phase.

A black SnS product was observed 15 min after the injection of the sulfur-oleylamine precursor into the tin precursor solution at 250 °C. The solid product was purified by centrifugation and imaged by transmission electron microscopy (TEM). Nanospheres with an average diameter of ~280 nm were obtained (Figure 1A and Supporting Information Figure S1). High-resolution TEM (HRTEM) images (Figure S1) of the edge of the nanospheres reveal a two-dimensional lattice with typical spacing of 0.21 nm, which corresponds to the distance between (220) lattice planes of the cubic zinc blende SnS (with a crystal constant of $a = 0.5845$ nm).[30] The X-ray diffraction (XRD) pattern (Figure 2A, black trace) indicates that the SnS nanospheres are zinc blende phase with trace amounts (~5%) of orthorhombic phase present.

The temperature of the reaction mixture was elevated to 330 °C at ~10 °C/min. After 10 additional minutes, intermediate SnS heterostructures with nanosphere heads and nanoribbon tails were observed (Figure 1B–D). High-resolution TEM (HRTEM) images (Figure 1E and Supporting Information Figures S2 and S3) reveal that the "head" area of the heterostructure consists of a two-dimensional (2D) lattice with a zinc blende spacing of 0.21 nm between (220) planes. The indexed fast Fourier transform (FFT) of a HRTEM image (inset in Figure 1E) reveals a typical hexagonal pattern, indicating the SnS nanosphere head is single-crystalline zinc blende phase projected along the ⟨111⟩ direction. In contrast, a HRTEM image of the "tail" section of the heterostructure (Figure 1F) shows a two-dimensional lattice with typical spacing of 0.29 nm, which corresponds to the distance between (101) planes of the orthorhombic phase of SnS (with a crystal constant of $a = 0.4329$ nm, $b = 1.1192$ nm, $c = 0.3894$ nm, JCPDS Card No. 39-0354). The indexed FFT of this HRTEM image (inset in Figure 1F) reveals a typical rhombic pattern, indicating that the SnS nanoribbon tail is single-crystalline orthorhombic phase projected along the ⟨010⟩ direction. These results clearly indicate the unique, dual-phase property of the intermediate heterostructures. Further characterization of the intermediate product by XRD (Figure 2A, red trace) confirms a mixture of zinc blende and orthorhombic SnS phases with a ~4:6 ratio. After 30 min at 330 °C, all of the metastable zinc blende SnS nanospheres were transformed into stable orthorhombic SnS nanoribbons, as shown in the TEM and scanning electron microscopy (SEM) images (Figure 1G–K and the Supporting Information Figures S4–S8). The XRD pattern of the final product (Figure 2A, blue trace) reveals a highly pure orthorhombic phase SnS with no zinc blende phase detected. Typical nanoribbons are 2–5 μm long, 150–500 nm wide, and ~10 nm thick.

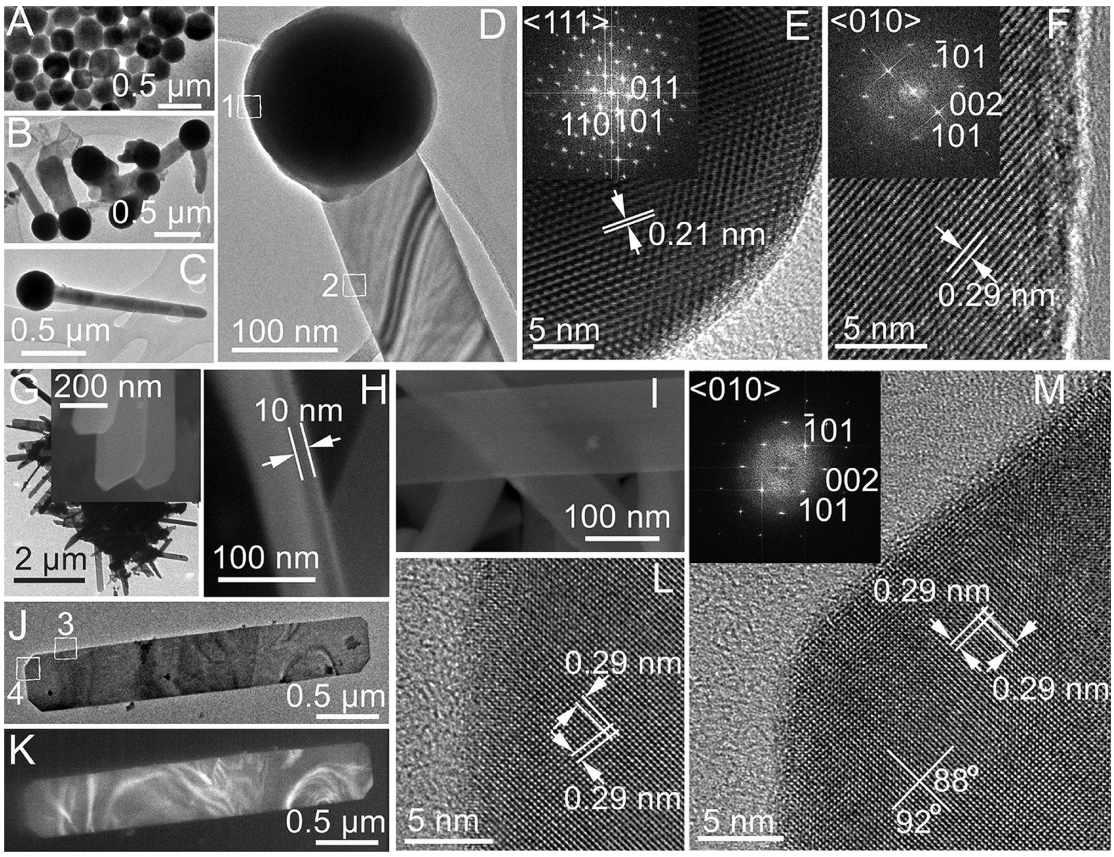

Figure 1. (A) TEM image of the initial zinc blende SnS nanospheres. (B−D) TEM images of the intermediate dual-phase SnS heterostructures, each containing a nanosphere head and a nanoribbon tail. (E,F) HRTEM images of the head and tail regions corresponding to the boxes marked "1" and "2" in (D); (inset in E,F) indexed FFTs of the images in E,F. (G) TEM image of the final orthorhombic SnS nanoribbons; (inset in G−I) SEM images of the final SnS nanoribbons. (J,K) Bright- and dark-field TEM images of a typical nanoribbon. (L,M) HRTEM images of the end and long edge corresponding to the boxes marked "3" and "4" in (J), respectively; (inset in M) indexed FFT of image M.

Bright-field and corresponding dark-field TEM images of a typical nanoribbon (Figure 1J,K) reveal that the nanoribbons are single-crystalline. HRTEM analysis (Figure 1L,M) of both the end and side of the nanoribbon shows the same 2D lattice composition with a spacing of 0.29 nm, which corresponds to the distance between (101) planes of the orthorhombic phase of SnS. The interplanar angles defined by the intersection of the (101) planes of the nanoribbon do not measure as 90°, but rather as 88 and 92° (Figure 1M), which is consistent with the calculated dihedral angle between (101) and (−101).[26] The indexed FFT of the HRTEM image (inset in Figure 1M) reveals a rhombic pattern, further confirming that the SnS nanoribbon is single-crystalline in the orthorhombic phase. These analyses confirm that the long edge of the nanoribbon is in the [001] direction with the terminating facets at the ends (001), along the sides (100), and on the faces (010). Mass calculations, before and after the phase transition, indicate that the average mass of a single SnS nanosphere (initial stage of the reaction) and a single SnS nanoribbon (final product) is nearly identical (details in the Supporting Information). This supports the view that the morphology change from nanosphere to nanoribbon is due to a zinc blende to orthorhombic phase transformation within the same nanostructure.

We observed that the reaction temperature plays a crucial role in the formation of nanoribbon morphology. When the temperature is held at 330 °C for the entire reaction, rather than using an initial temperature of 250 °C, 2D orthorhombic nanosheets with 200−500 nm edges and 30−60 nm thicknesses were obtained, as shown in Supporting Information Figure S9. We propose that the zinc blende nanospheres initially formed at a lower temperature act as templates and limit the final dimensions of the nanoribbons formed during the phase transition at higher temperatures. To our knowledge, the formation of single-crystal SnS nanoribbons by a metastable-to-stable phase transition has never been reported. Odom and co-workers reported a SnS phase transition from zinc blende tetrahedral- shaped crystals to 2D orthorhombic nanosheets;[30] however, no intermediate dual-phase heterostructures were observed. One literature report[38] detailed the formation of single-crystalline Sb_2Se_3, $Sb_2Se_{3-x}S_x$ ($0 < x < 3$) and Sb_2S_3 nanotubes following a transition from amorphous nanospheres to

orthorhombic nanotubes. It is well-known that the phase transition of a solid material results in changes to the material properties, which play an important role in a variety of processes ranging from information storage to materials processing.[39−41] In the field of semiconductor crystal growth and engineering, phase transitions from the metastable phase to the stable phase have been utilized as a novel practical route to synthesize new semiconductor materials.[42,43]

For SnS, the phase transition between metastable zinc blende phase and stable orthorhombic phase is still largely unexplored. We believe that the following two factors may play important roles in the phase transition of SnS nanocrystals: the small size of the nanocrystals and the particular surface modifications. First, size-dependent crystalline phase transitions, which can be considered as an intrinsic property of nanocrystals, exist for a wide range of materials.[44] Decreasing the size of the nanocrystals has a significant influence on the phase transition by modifying the transition energies and thus the transition temperatures. For example, the metastable zinc blende nanocrystals generated at lower temperatures can be transformed into the stable orthorhombic phase at moderately higher temperatures.[30] This is likely because the formation of the metastable zinc blende phase nanospheres is kinetically faster and dominates at lower temperatures. With a relatively lower energy barrier for the phase transition, the metastable zinc blende nanospheres can be transformed to the stable orthorhombic phase by providing the additional thermal energy. Second, by adsorbing and desorbing the capping ligand, oleylamine, on the surface of the SnS nanocrystals, the surface and/or interface energy can be modified, subsequently affecting the phase transition energy. We expect that studying the unique phase transitions in SnS nanocrystals will lead to better understanding of the mechanism behind the transitions and to new strategies for the synthesis of novel nanomaterials.

UV−vis−NIR absorption spectroscopy was used to determine the optical properties of the SnS products at various synthesis stages (Figure 2B). The absorption onset of the initial zinc blende SnS nanospheres occurs around 760 nm, while the absorption onset begins around 1015 nm for the final orthorhombic phase SnS nanoribbons. The intermediate product showed the two onsets of absorption close to 760 and 1015 nm, consistent with its dual-phase heterostructure. To determine the direct and indirect band gap values, Kubelka−Munk transformations were performed. A plot of $[F(R)h\nu]^2$ *versus* energy indicates a direct band gap of 1.66 and 1.27 eV for the nanospheres and nanoribbons, respectively (Figure 2C), while a plot of $[F(R)h\nu]^{0.5}$ *versus* energy indicates an indirect band gap of 1.48 and 1.18 eV for the nanospheres and nanoribbons, respectively (Figure 2D). These values match well

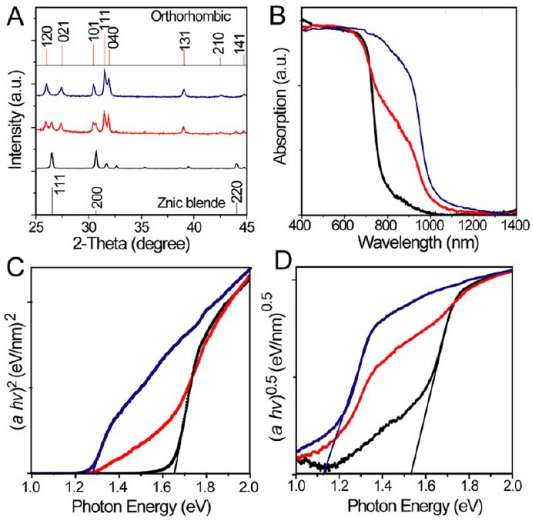

Figure 2. (A) Powder XRD pattern of the initial SnS nanospheres (black trace), the intermediate SnS heterostructures (red trace), and the final SnS nanoribbons (blue trace). The red vertical bars along the top are indices of the orthorhombic phase of SnS crystals according to JCPDS card No. 39-0354. The black vertical bars along the bottom are indices of the zinc blende phase of SnS crystals according to literature.[30] (B−D) UV−vis−NIR absorption spectra, plots of $(ah\nu)^2$ and $(ah\nu)^{0.5}$ *versus* photon energy ($h\nu$) of the initial SnS nanospheres (black trace), the intermediate SnS heterostructures (red trace), and the final SnS nanoribbons (blue trace). The spectra were recorded from powder samples drop-cast at room temperature on a glass slide using a UV−vis−NIR spectrometer equipped with an integrating sphere.

with previously reported results for SnS.[16] Little quantum confinement effects were observed, possibly due to the relative large dimension of the nanoribbon obtained compared to the small Bohr radius of SnS ~7 nm.[35]

Individual, single-crystal SnS nanoribbon based optoelectronic devices were fabricated and studied in an inert gas (N_2 or argon) environment using a back-gated FET configuration as shown in Figure 3A,B. The details of device fabrication and characterizations are given in the materials and methods section. Briefly, single nanoribbons were deposited on the surface of a highly doped n-type Si substrate covered with a 300 or 100 nm thick SiO_2 dielectric layer. The electrodes are composed of Cr (30 nm) and Au (120 or 150 nm), where Cr has a work function of 4.50 eV, close to that of orthorhombic SnS (4.2 eV).[45] Ten devices were fabricated (see Figure S10) and characterized. Curves of source−drain current (I_{ds}) *versus* source−drain voltage (V_{ds}) were measured, and typical $I_{ds}-V_{ds}$ curves at $V_{gs} = 0$ for the nanoribbons are shown in Figure 3C. A zero current region is visible at low voltage bias, suggesting the existence of an energy gap. The band gap of the SnS nanoribbon was determined to be 1.3 eV from the dI_{ds}/dV_{ds} *versus* V_{ds} curve (inset in Figure 3C), which is close to the direct band value of the SnS nanoribbons obtained from the optical absorption study (Figure 2B).

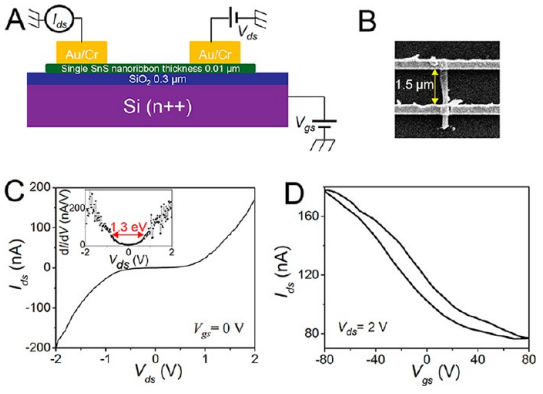

Figure 3. (A) Schematic of a single SnS nanoribbon based field-effect transistor device. (B) SEM image of a typical device. The distance between two electrodes is 1.5 μm, and the width of the ribbon is about 200 nm. (C) I_{ds} *vs* V_{ds} curve of a typical single SnS nanoribbon FET device in the dark at V_{gs} = 0 V. Top left inset in (C) shows the derivative of the $I-V$ curve with band gap energy of 1.3 eV. (D) I_{ds} *vs* V_{gs} in the dark at V_{ds} = 2.0 V of the same single nanoribbon based FET device shown in (B), exhibiting p-type semiconductor behavior.

Figure 3D shows I_{ds} *versus* V_{gs} at V_{ds} = 2 V for the same device shown in Figure 3B. We observed the source−drain current decrease with an increase in the gate potential, suggesting that the holes, rather than electrons, are the major carriers inside the SnS nanoribbon. Thus, the SnS nanoribbon based device displays p-type behavior. A small hysteresis was observed, likely originating from the water present in the atmosphere or charged impurities and contamination (such as amorphous carbon) that were incorporated during the FET device fabrication process. The transconductance g_m (=dI_{ds}/dV_{gs}) was acquired by fitting the linear region of the I_{ds} *versus* V_{gs} curve. With the backgate area capacitance known and the dimensions of the nanoribbons measured from the SEM images, the hole mobility for this device was calculated based on the equation[46]

$$\mu = L/(W \times C_{ox} \times V_{ds}) \times dI_{ds}/dV_{gs} \quad (1)$$

For the specific device reported here, the channel length L is 1.5 μm, the channel width W is 0.21 μm, the capacitance C_{ox} is $\varepsilon_o\varepsilon_r/d$ (ε_0 is 8.854 × 10^{-12} Fm^{-1}, ε_r for SiO_2 is 3.9, and d is the thickness of SiO_2 ~300 nm), V_{ds} is 2 V, and dI_{ds}/dV_g obtained from the slope of the plot of I_{ds} *versus* V_g is −1.23 nA/V, as shown in Figure 3D. The calculated hole mobility μ of this device is *ca.* 0.4 cm^2 V^{-1} s^{-1}.

The hole concentration in the nanoribbon can be estimated by $n_h = \sigma/e\mu_h$, where σ is the conductivity (defined as the inverse of the resistivity $\rho = R \times S/L$ = 1.4 Ωcm, here R is $2V/200$ nA = 1× 10^7 Ω, S is the vertical cross-section area of nanoribbon = 10 nm × 210 nm = 2.1 × 10^{-11} cm^2, and L is the length between the electrodes 1.5 μm), e is the charge of an electron 1.6 × 10^{-19} C, and μ_h is the calculated hole mobility. Thus, the hole concentration is calculated as 1.1 × 10^{19} cm^{-3}. The p-type semiconductor behavior of the SnS nanoribbon might be due to a small amount of Sn^{2+} that is substituted by Sn^{4+}. Derived from the calculated hole concentration, the substitution rate in the SnS nanoribbons is estimated to be ~0.025%, a value that is too low to be detected using XPS or EDS.

The FET measurements were repeated on six individual devices (fabricated with the as-synthesized nanoribbons) and revealed calculated hole mobilities ranging from 0.2 to 1.1 cm^2 V^{-1} s^{-1} (see Figure S11). There are options to improve the hole mobility of the colloidal single SnS nanoribbon based FET devices. For example, a top-gate FET configuration where a high dielectric gate material like HfO_2 is deposited on top of SnS nanoribbons could be used, as demonstrated in the single-layer MoS_2 based top-gate FET devices.[12] It should be noted that the hole mobility of the single SnS nanoribbon FET device achieved here is comparable to the best known solution-processed organic[47] and nanocrystal[48−50] devices reported to date, and also at the same level as that of other IV−VI PbS and PbTe nanowire FET devices where the nanowires are synthesized by the chemical vapor transport (CVT) method.[51]

Figure 4A shows the configuration of a SnS single nanoribbon photodetector for photocurrent measurements. The photoswitching characteristics and stability of single SnS nanoribbon based photodetectors were investigated in air at room temperature. Three different color lasers (532 nm light with a power intensity of 50 mW cm^{-2}, 650 nm light with 38 mW cm^{-2}, and 405 nm light with 13 mW cm^{-2}) were used as the light source for the device. The steady-state photocurrent (under constant light illumination) was recorded while the source−drain voltage was varied between −3 and +3 V (Figure 4B). The device responded to all wavelengths of light, displaying increased current as compared to that in the dark. This is due to the small direct band gap energy (1.27 eV) of the SnS nanoribbons, where the electron hole pairs could be excited by all photons in the visible range. We found that the photocurrent generated from the single SnS nanoribbon photodetector depends on the power intensity of the illuminating light. Figure 4C shows the current−voltage ($I-V$) curves when the power intensity (P_{light}) is increased from 0, 9, 50, 67, to 120 mW cm^{-2}. Plots of photocurrent (I_{ph}, the current difference with the light ON and OFF) as a function of P_{light} are shown in Figure 4D. The dependence of the photocurrent on light intensity can be fit to a power law, $I_{ph} \sim P_{light}^{\theta}$, where θ determines the response of the photocurrent to light intensity.[8] The fitting reveals a linear relationship with $\theta \sim 0.99$ for V_{ds} = 3 V, 0.95 for V_{ds} = 2 V, and 0.93 for V_{ds} = 1 V. In such a single SnS nanoribbon based photodetector, the power law dependence of I_{ph} on P_{light} further confirms that the photocurrent is

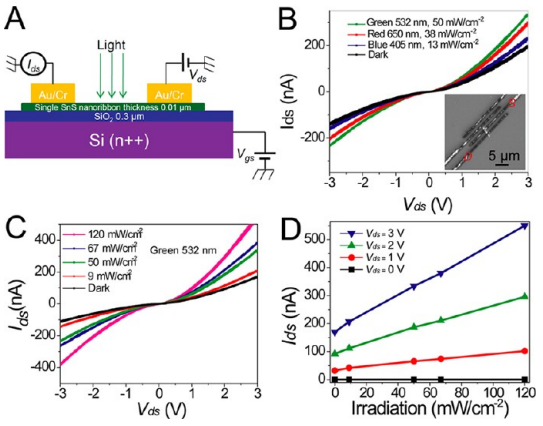

Figure 4. (A) Schematic illustration of the single SnS nanoribbon based photodetector device configuration for photocurrent measurements. V_{ds} is held between 0 and 3 V, V_{gs} is held at 0 V, and I_{ds} (between the source and drain electrodes) is monitored as light is irradiated on and off the nanoribbon surface. The laser spot is 4 mm in diameter with the irradiation controlled by clipping with a light block. (B) Typical output characteristics of the photodetector at different wavelengths of illumination: 650 nm (red), 532 nm (green), and 405 nm (blue) at V_g = 0 V. (C,D) Typical drain current (I_{ds}) and photocurrent (I_{ph}) *vs* drain voltage (V_{ds}) of the photodetector at different illuminating optical powers of 532 nm green light with P_{light} ranging from 9 to 120 mW cm^{-2} at V_g = 0 V. Inset in (B) shows an optical image of a typical photodetector device.

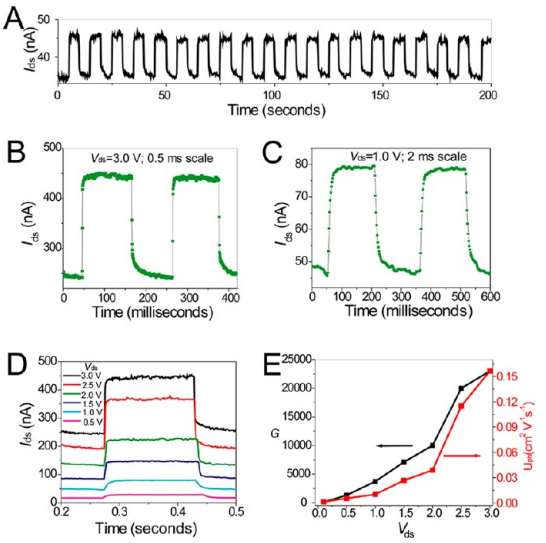

Figure 5. (A) Stability of the photoswitching behavior of single SnS nanoribbon photodetectors at V_{ds} = 1 V, using 532 nm light of power intensity P_{light} = 90 mW cm^{-2}. (B,C) Rise and decay rate of the photocurrent for a single SnS nanoribbon photodetector measured at V_{ds} = 3.0 V with 0.5 ms time resolution and V_{ds} = 1.0 V with 2 ms time resolution. The rise and decay time (τ_R and τ_D) for the rise edge and decay edge of the photocurrent were obtained by fitting the curve with a single exponential equation. (D) One cycle of a single SnS nanoribbon photodetector at different drain voltages (V_{ds} = 0.5 to 3 V) under 90 mW cm^{-2} illumination. (E) Plots of the calculated gain (G) *vs* drain voltages, and the mobility of the photon-generated holes (μ_{ph}) *vs* drain voltage. As the drain voltage increases, both the G and μ_{ph} increase.

determined by the amount of photon-generated carriers under illumination.

Under intermittent illumination, the current ramps to a high steady value (ON state) with light and resumes to the low value (OFF state) under dark. The stability of the photoswitching behavior was demonstrated by performing repeating pulsed illuminations on the device for 200 s. Steady photocurrent levels were observed after >2000 cycles of switching (Figure 5A and Figure S12). The switching behavior was also investigated using different optical powers and drain voltages (Figure 5D). With an optical power of approximately 90 mW cm^{-2}, the photocurrent increases from 0.8 to 200 nA as the drain voltage increases from 0.1 to 3.0 V. The dependence of photocurrent on the drain voltage indicates that not all photon-generated charge carriers can be converted to the photocurrent observed, due to recombination of the charge carriers in the nanoribbon. A larger drain voltage can drive photon-generated charge carriers to reach the electrodes faster (resulting in decreased carrier transit time in the semiconductor device), thus suppressing recombination of photon-generated charge carriers. With a zero gate voltage, the photoresponsivity of the single SnS nanoribbon photodetector can reach 3 μA/W cm^{-2} under illumination with a low optical power (90 mW cm^{-2}) and a small drain voltage (V_{ds}, 3 V).

The ON−OFF photoswitching time is a key parameter that determines the capability of a photodetector to follow a fast-varying optical signal. Figure 5B,C shows the photoswitching behavior of single SnS nanoribbon based photodetectors with the change of photocurrent recorded on short time scales. For intrinsic semiconductors, recombination is considered as a monomolecular process, and the recombination rate is proportional to the excess of charge carriers, given by[52]

$$d\Delta n/dt = g_n - \Delta n/\tau_n \quad (2)$$

where g_n is the generation rate of charge carriers, Δn is the concentration of the excess electrons (or holes) created in the conduction or valence bands by photon excitation, and τ_n is the lifetime of charge carriers.[52] Assuming that τ_n is independent of n, and the electron−hole pairs are generated by direct band gap excitation, $I = I_0(1 - e^{-t/\tau R})$ and $I = I_0 e^{-t/\tau D}$ for the photocurrent (I) at the rise (time constant τ_R) and decay (time constant τ_D) edges, respectively. Both the rise and decay edges of the SnS nanoribbon device were well fit by the above exponential equations. As shown in Figure 5B, the observed typical switching time constants for the current rise (0.94 and 0.98 ms from OFF to ON) or decay (1.09 and 1.13 ms from ON to OFF) process are on the millisecond scale.

Figure S13 illustrates the rise and fall edges, respectively, of the photocurrent for the ON and OFF state of irradiation at different drain voltages. We observed that both the rise and decay time decreases with

TABLE 1. Summary of the Calculated Gain (G), Transit Time (t_{tran}), and Mobility of the Photon-Generated Holes (μ_{ph}) at Different Drain Voltages of the SnS Single Nanoribbon Devices

V_{ds} (V)	I_{ph} (nA)	τ_D (ms)	G	t_{tran} (μs)	μ_{ph} (cm^2 V^{-1} s^{-1})
3.0	200	1.1	23000	0.048	0.16
2.5	170	1.5	20000	0.077	0.12
2.0	90	3.0	10000	0.29	0.039
1.5	62	4.0	7100	0.56	0.027
1.0	32	8.1	3700	2.2	0.010
0.5	11	10.5	1300	8.1	0.0055
0.1	0.8	14.4	92	160	0.0014

increasing drain voltage. The average rise/decay times are 0.96/1.11, 1.23/1.51, 2.72/3.00, 3.69/3.98, 7.50/8.13, 9.66/10.47, and 12.64/14.42 ms for the drain voltage of 3.0, 2.5, 2.0, 1.5, 1.0, 0.5, and 0.10 V, respectively. For all drain voltages, the rise time is always shorter than the corresponding decay time, which results in asymmetric curves at the rise and fall edges.

The photocurrent gain (G), defined as the number of electrons collected by electrodes due to excitation per photon, can be expressed as[52]

$$G = N_e/N_p = \tau_D/t_{tran} \quad (3)$$

where N_e is the number of electrons collected in a unit time, N_p is the number of photons absorbed in a unit time, τ is the carrier lifetime obtained from τ_R or τ_D, and t_{tran} is the transit time of the charge carrier in the channel material between the electrodes. In the experiment shown in Figure 5B, the photocurrent is approximately 200 nA for a 3 V drain voltage, the light intensity is 90 mW cm^{-2} at 532 nm, and the surface area of the nanoribbon is 2.25 $\times$ 10^{-9} cm^2. If the absorption coefficient[53] is approximately 1 $\times$ 10^5 cm^{-1}, and the thickness of the device is 10 nm, then 10% of the light illuminated on the nanoribbon is absorbed.[54] Therefore, the gain of nanoribbon photoconduction G is calculated to be $\sim$2.3 $\times$ 10^4 according to eq 3.

From eq 3, if the decay time (τ_D) is 1.1 ms, the transit time of the charge carriers between the electrodes, t_{tran}, is 48 ns for a 3 V drain voltage. According to Bube *et al.*,[51] if the photoconductivity gain for a given material is calculated, and the carrier lifetime is known from steady-state data, the mobility of the photon-generated carriers can be calculated according to

$$\mu_{ph} = L^2/(t_{tran} \times V_{ds}) \quad (4)$$

where V_{ds} is the applied drain voltage, L is the channel distance (1.5 μm) of the photodetector, and t_{tran} is the transit time. The mobility of the photon-generated carrier μ_{ph} at 3 V drain voltage is calculated as 0.16 cm^2 V^{-1} s^{-1}. For different drain voltages (from 0.1 to 3 V), the calculated gain G, transit time t_{tran}, and mobility of the photon-generated holes μ_{ph} are listed in Table 1 and plotted in Figure S13. We observe that as the drain voltage increases, I_{ph}, G, and μ_{ph} also increase, while τ_D and t_{tran} decrease.

In a single SnS nanoribbon photodetector, the absorption of photons will excite electrons from the valence to conduction band, where the electrons and holes are separated across the SnS nanoribbon energy band gap. If there are surface traps to remove the electrons, then excess holes are generated in the nanoribbon photodetector. The faster photoswitching speed (up to $\sim$1 ms) of SnS nanoribbons compared to SnS thin films and bulk crystals (rise time of 120 s or more[55]) could be attributed to the single-crystal structure of the SnS nanoribbons. First, the density of traps induced by defects inside the nanoribbon is drastically reduced, thus the photocurrent reaches a steady state rapidly in both the rise and decay stages. In addition, the ultrathin thickness of the SnS nanoribbons reduces the energy barrier for the carrier to cross the interface of the semiconductor nanoribbons and metallic electrodes (Au/Cr) due to less profound band bending at the semiconductor and metal (electrode) interface.[8] As a result, the high photocurrent is generated with a fast rise and decay lifetime. The ON/OFF ratio of the current for the SnS nanoribbon based photodetector is about 1.8, with V_{ds} ranging from 0.5 to 3 V, exhibiting a small voltage dependence. When the drain voltage is further decreased, the dark and light current both become too low to be measured. The ON/OFF ratio for the photodetector reported here is lower than reported by Yin *et al.*, who used inert gas protection and thermal annealing treatment after the nanodevice fabrication.[46]

It is well-known that organic ligands with long hydrocarbon chains are essential to capping the surface of nanomaterials to facilitate size and shape control during colloidal synthesis. However, these ligands may act as an insulating layer between semiconductors and electrodes, preventing effective charge transfer. We employed a ligand exchange strategy to replace the long chain organic ligands with short inorganic chalcogenide ligands yielding completely inorganic semiconductor nanomaterials. Impressively high carrier mobilities have been reported for field-effect transistor devices composed of semiconductor quantum dot arrays, such as CdSe/ZnS nanocrystals, after similar ligand exchange treatment.[36]

In a typical ligand exchange process, we combined a solution of oleylamine-capped SnS nanoribbons in nonpolar hexane with a solution of inorganic HS^- ligands in polar formamide. The two-phase mixture containing immiscible layers of formamide and hexane was vortexed for about 30 min. After settling, complete transfer of the nanoribbons from the nonpolar solvent to formamide was observed (Figure 6A). Fourier transform infrared spectroscopy (FTIR) spectra of SnS nanoribbons taken before and after the ligand exchange (Figure 6B) show that the transfer of nanoribbons from

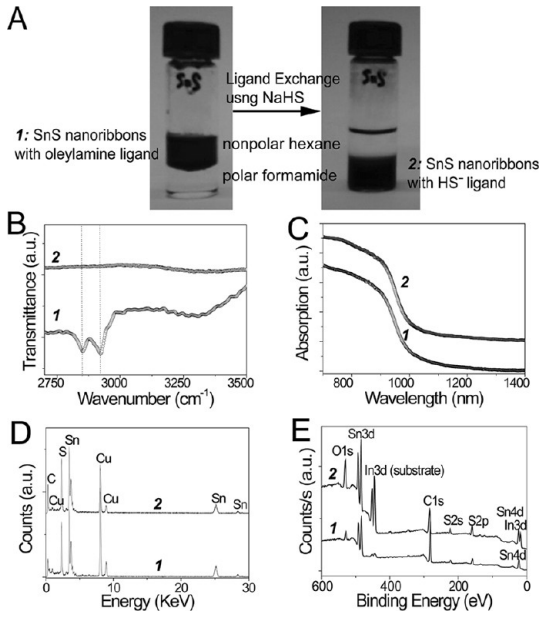

Figure 6. (A) Colloidal dispersion of SnS nanoribbons undergoes transfer from an upper, nonpolar hexane layer (density: 0.659 g/mL at 25 °C) to a lower polar, formamide layer (density: 1.134 g/mL at 25 °C) upon exchange of the original oleylamine ligands with HS^- ligands. (B–E) FTIR, UV–vis–NIR absorption, EDS and XPS spectra of SnS nanoribbons before ligand exchange (curves 1) and after ligand exchange (curves 2), respectively.

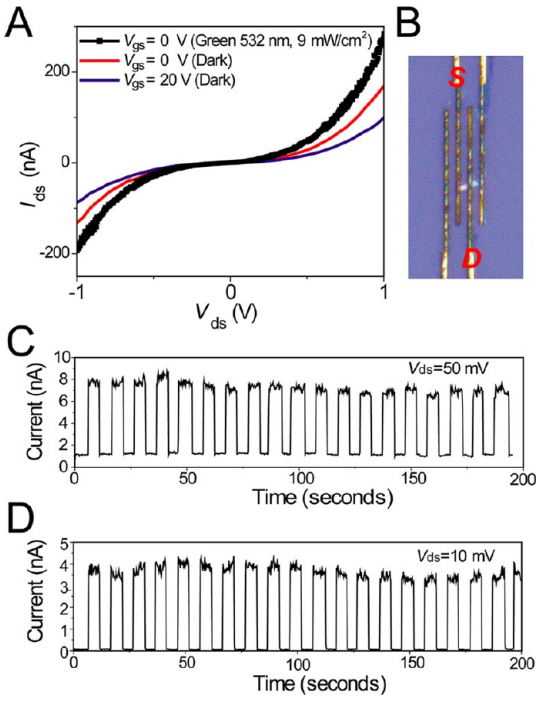

Figure 7. (A) Typical output characteristics of SnS nanoribbon based photodetectors at difference gate voltages (V_{gs} = 0, 20 V) under dark or illuminated with 532 nm light of power intensity P_{light} = 9 mW cm^{-2} at V_{gs} = 0 V. (B) Optical image of the single SnS nanoribbon photodetector device with labeled source and drain electrodes. (C,D) Stability test of the photoswitching behavior of single SnS nanoribbon photodetectors at V_{ds} = 50 mV and 10 mV, illuminated with 532 nm light of power intensity P_{light} = 90 mW cm^{-2}. The ON/OFF ratio of the current is ~8 at 50 mV and ~80 at 10 mV.

hexane to formamide resulted in complete disappearance of the bands at 2852 and 2922 cm^{-1}, corresponding to C–H stretching in the original organic oleylamine ligands.[36] These results confirm that the original organic oleylamine ligands were completely removed by the HS^- ligands and all-inorganic colloidal SnS nanoribbons were obtained. UV–vis–NIR absorption spectra of the SnS nanoribbons (Figure 6C) showed no change before and after the ligand exchange, implying no changes in the size or shape of the nanoribbons. Energy-dispersive X-ray spectroscopy (EDS) spectra of the SnS nanoribbons capped with oleylamine ligands and HS^- are presented for comparison in Figure 6D. The increase in the S/Sn ratio from 0.98:1 to 1.03:1 suggests the existence of a HS^- ligand layer on the surface of SnS nanoribbons after the exchange. In addition, survey X-ray photoelectron spectra (XPS) of the SnS nanoribbons revealed that the atomic ratio of S/Sn for SnS nanoribbons with OAm ligand is 0.98:1, while the atomic ratio is 1.08:1 with the HS^- ligand (see Figure 6E), consistent with the EDS analysis. As shown in Figure S14, the peak at 485.9 eV corresponds to the binding energy of Sn^{2+} $3d_{5/2}$, and the corresponding binding energy of S^{2-} $2p_{3/2}$ is 161.2 eV. No evidence of Sn^{4+} (binding energy at 486.7 eV) is detected in the spectra.

As shown in Figure S11, we found that that after the surface ligand exchange to remove the insulating organic layer on the surface of the nanoribbon, the charge carrier mobility of the device is significantly improved to about 4 times in dark. The performance of the HS^- ligand-coated nanoribbon based photodetector was analyzed, as shown Figure 7. Similar to the SnS nanoribbon based device before the ligand exchange, the all-inorganic device responded to the illumination of green light (532 nm light with power intensity P_{light} = 9 mW cm^{-2}), displaying increased current as compared to that in the dark. As the gate potential was increased the source–drain current decreased, suggesting that the HS^- ligand-coated SnS nanoribbon based device also displays p-type behavior. Under intermittent illumination with power intensity P_{light} = 90 mW cm^{-2}, the current ramps to the ON state with light and resumes to the OFF state in the dark. A steady level of photocurrent was observed by applying repeating pulsed illuminations on the device for 200 s, which demonstrated the stability of the switching behavior (Figure 7C,D and Figure S15). The ON/OFF ratio of the current was ~2–3 with the drain voltage ranging from 0.5 to 3 V but was increased to approximately 8 as the drain voltage was decreased to 50 mV (at V_{gs} = 0 V) (Figure 7C) and reached ~80 when the drain voltage was further decreased to 10 mV (Figure 7D). When the power intensity of the 532 nm light was reduced to 45 mW cm^{-2} (see Figure S15), the ON/OFF ratio

dropped to ~40 for the same device operated under identical conditions. We found that removal of the insulating surface ligand greatly improves the contact of the electrodes to the nanoribbons, thereby increasing the photocurrent which allows the device to be operated using very small drain voltages (<10 mV). Overall, the performance of our solution-processed single SnS nanoribbon photodetector is comparable to the best photodetectors reported, including single CdSe nanoribbons,[52] single CdS nanoribbon,[56] PbS nanocrystals,[57] *etc.*[8]

CONCLUSION

In summary, we present the controlled colloidal synthesis of high-quality single-crystalline SnS nanoribbons through a metastable-to-stable phase transition process. Optical measurements show that the onset of absorption of the initial ZB nanospheres occurs at 760 nm (1.63 eV), while the absorption begins at 1015 nm (1.22 eV) for the final orthorhombic phase nanoribbons. Simple norganic HS^- ligands were used to successfully replace the original organic oleylamine ligand. The photoconductive characteristics of SnS single nanoribbons were investigated, which demonstrate highly sensitive and rapid response to illumination by blue, green, and red light at room temperature. Switching between photocurrent generation and annihilation is complete within 1 ms and is accompanied by high photoconductivity gains (up to 2.3×10^4). The ON/OFF ratio of the photodetector can be engineered to 80 (4 nA/50 pA) using a small drain current (10 mV). We found that the drain voltage has a significant influence on the photoswitching speed with higher voltages exhibiting faster photoswitching rates. These desirable properties can be attributed to the high single-crystal quality and large surface-to-volume ratio of the ultrathin SnS nanoribbons. This work reinforces the potential application of low-cost, less toxic, and earth-abundant IV–VI colloidal semiconductor nanostructures in optical, electronic, and optoelectronic devices.

MATERIALS AND METHODS

Materials and Synthesis. Tin(IV) iodide (SnI_4, anhydrous, powder, 99.999%), sulfur (S, powder, 99.998%), oleylamine (OAm, 70% tech.), hexamethyldisilazane (HMDS, >99%), sodium hydrosulfide (NaHS, ≥90%), formamide ($HCONH_2$, ≥99.5%), hexane (≥95%), isopropyl alcohol (IPA, 99%), methanol (≥99.5%), and ethanol (99%) were purchased from Sigma-Aldrich and used without further purification. In a typical experiment, S-OAm precursor solution was prepared in a flask, where 64 mg (2 mmol) of sulfur powder was mixed with 20 mL of OAm, and stirring under low vacuum (100 mtorr) was performed in order to remove moisture and O_2; the solution was subsequently heated at 100 °C for 2 h before use. Then, 63 mg (0.10 mmol) of SnI_4, 10 mL (~31 mmol) of OAm, and 2 mL (9.4 mmol) of HMDS were added to a separate 100 mL three-neck round-bottom flask with stirring, and the solution was heated to 100 °C and degassed under 100 mTorr pressure for 30 min. HMDS was essential to the formation of the uniform size SnS nanocrystal products. We found that, if no HMDS present, the sample will show poor crystallinity (or amorphous) with very broad size distribution. Next, the flask was filled with N_2, and the solution was heated to ~250 at 10 °C/min, and 1 mL of S-OAm precursor solution was swiftly injected. Timing was started immediately after injection, and the growth temperature was maintained at 250 °C. After 15 min, the yellowish solution turned black. At this point, the reaction temperature was increased to 330 °C at ~10 °C/min. After remaining at this temperature for 30 min, the reaction was stopped by injection of the hot black reaction solution (2 mL) into a mixture of methanol (6 mL), ethanol (6 mL), and IPA (6 mL) at room temperature. The resulting product was centrifuged at 15 000*g* and 4 °C for 30 min, redispersed in hexane (2 mL), and washed in a mixture of methanol, ethanol, and IPA (1:1:1) three times by centrifugation. The final product was redispersed in hexane (2 mL) for optical measurements and structural characterization. The overall yield of the SnS nanoribbons is estimated to be 60% by comparison of the mass of final product and initial source materials used.

Ligand Exchange. The ligand exchange process was carried out in air. Colloidal dispersions of SnS nanoribbons with organic ligands were prepared in nonpolar hexane, while solutions of inorganic ligands were prepared in polar formamide, immiscible with hexane. For a typical ligand exchange, 0.5 mL of SnS nanoribbons solution (2 mg/mL) was mixed with 1 mL of NaHS solution (5 mg/mL). The mixture was vortexed for 10–30 min, leading to a complete phase transfer of SnS nanoribbons from hexane to formamide phase. The phase transfer can be monitored by the color change of hexane (black to colorless) and formamide (colorless to black) phases. The formamide phase was separated out by carefully removing the top hexane layer by a syringe, then followed by more washing steps: adding more hexane (hexane/formamide 1:1 volume ratio), mixing them by vortex, settling and removing the top hexane layer by a syringe. We did not observe any oxidation and dissolution during the ligand exchange process.

Characterizations. Bight and dark filed transmission electron microscopy (TEM), high-resolution TEM (HRTEM), selected area electron diffraction (SAED), and energy dispersive X-ray spectroscopy (EDS) were performed on a JEOL JEM 2010F electron microscope operating at 200 kV using ultrathin carbon-coated 400 mesh copper grids or lacey carbon-coated copper grids (Ted Pella) as the sample substrates. Scanning electron microscopy (SEM) was performed using silicon as the sample substrate on a FEI FIB/SEM Nova 200 NanoLab. Powder X-ray diffraction (XRD) measurements employed a PANalytical X'Pert Pro Materials Research X-ray diffractometer with Cu Kα radiation (λ = 1.5418 Å) and scanned at a rate of 0.025 deg/s. Ultraviolet–visible–near-infrared (UV–vis–NIR) absorption spectra were recorded at room temperature with a JASCO V-670 spectrophotometer equipped with an integrating sphere (model ISN-723, diameter = 60 mm). Samples for XRD and UV–vis–NIR absorption characterization were prepared by drop-coating concentrated nanocrystal samples in isopropyl alcohol or hexane onto a clean glass substrate and dried in air. Fourier transform infrared spectroscopy was measured with a Thermo Nicolet 6700 FTIR (Thermo Fisher Scientific, MA) equipped with Smart orbit (a diamond single-bounce ATR accessory). The powders of the SnS nanoribbons before and after ligand exchange were deposited on the indium sample holder and examined with an X-ray photoelectron spectroscopy (XPS) system consisting of an Al monochromator and twin anode sources.

Device Fabrication and Measurements. Metal (Au) markers for position registration were first fabricated by electron beam lithography (EBL) on n-type silicon substrates with 300 nm thermal silicon dioxide. The SnS nanoribbons were dispersed

in hexane (before ligand exchange) or ethanol (after ligand exchange) and transferred to the substrates by a pipet. The nanoribbons remained on the SiO_2 surface after the solvent evaporation. After determining the position of each nanoribbon by SEM with the aid of metal markers, source–drain electrodes (30 nm Cr and 120 nm/150 nm Au) were fabricated by EBL. The electrical measurements were conducted with a Keithley 2636A in a faraday cage under N_2 or argon gas protection. The hole mobility is calculated to be 0.4 ± 0.1 $cm^2\ V^{-1}\ s^{-1}$ with nanoribbons before ligand exchange and improved to 0.9 ± 0.2 $cm^2\ V^{-1}\ s^{-1}$ with ribbons after ligand exchange. Multiple devices (>10) have been fabricated (see Figure S10) and measured to obtain the reproducible results. All photocurrent measurements were performed in air and at room temperature.

Conflict of Interest: The authors declare no competing financial interest.

Acknowledgment. This research was supported by grant from ONR to Y.L. and Z.D. We thank Dr. J. Nangreave for proof-reading the manuscript. We thank M. Dodson for help with FTIR measurements. The use of facilities within the Center for Solid State Science (CSSS) and Center for Solid State Electronics Research (CSSER) at ASU is also acknowledged.

Supporting Information Available: Additional characterization details. This material is available free of charge *via* the Internet at http://pubs.acs.org.

REFERENCES AND NOTES

1. Han, M. Y.; Ozyilmaz, B.; Zhang, Y. B.; Kim, P. Energy Band-Gap Engineering of Graphene Nanoribbons. *Phys. Rev. Lett.* **2007**, *98*, 206805.
2. Li, X. L.; Wang, X. R.; Zhang, L.; Lee, S. W.; Dai, H. J. Chemically Derived, Ultrasmooth Graphene Nanoribbon Semiconductors. *Science* **2008**, *319*, 1229–1232.
3. Chen, Z. G.; Zou, J.; Liu, G.; Li, F.; Wang, Y.; Wang, L. Z.; Yuan, X. L.; Sekiguchi, T.; Cheng, H. M.; Lu, G. Q. Novel Boron Nitride Hollow Nanoribbons. *ACS Nano* **2008**, *2*, 2183–2191.
4. Zeng, H. B.; Zhi, C. Y.; Zhang, Z. H.; Wei, X. L.; Wang, X. B.; Guo, W. L.; Bando, Y.; Golberg, D. "White Graphenes": Boron Nitride Nanoribbons *via* Boron Nitride Nanotube Unwrapping. *Nano Lett.* **2010**, *10*, 5049–5055.
5. Schwierz, F. Graphene Transistors. *Nat. Nanotechnol.* **2010**, *5*, 487–496.
6. Higginbotham, A. L.; Kosynkin, D. V.; Sinitskii, A.; Sun, Z. Z.; Tour, J. M. Lower-Defect Graphene Oxide Nanoribbons from Multiwalled Carbon Nanotubes. *ACS Nano* **2010**, *4*, 2059–2069.
7. Kosynkin, D. V.; Lu, W.; Sinitskii, A.; Pera, G.; Sun, Z. Z.; Tour, J. M. Highly Conductive Graphene Nanoribbons by Longitudinal Splitting of Carbon Nanotubes Using Potassium Vapor. *ACS Nano* **2011**, *5*, 968–974.
8. Zhai, T.; Li, L.; Wang, X.; Fang, X. S.; Bando, Y.; Golberg, D. Recent Developments in One-Dimensional Inorganic Nanostructures for Photodetectors. *Adv. Funct. Mater.* **2010**, *20*, 4233–4248.
9. Kind, H.; Yan, H. Q.; Messer, B.; Law, M.; Yang, P. D. Nanowire Ultraviolet Photodetectors and Optical Switches. *Adv. Mater.* **2002**, *14*, 158–160.
10. Soci, C.; Zhang, A.; Bao, X. Y.; Kim, H.; Lo, Y.; Wang, D. L. Nanowire Photodetectors. *J. Nanosci. Nanotechnol.* **2010**, *10*, 1430–1449.
11. Sinitskii, A.; Dimiev, A.; Corley, D. A.; Fursina, A. A.; Kosynkin, D. V.; Tour, J. M. Kinetics of Diazonium Functionalization of Chemically Converted Graphene Nanoribbons. *ACS Nano* **2010**, *4*, 1949–1954.
12. Radisavljevic, B.; Radenovic, A.; Brivio, J.; Giacometti, V.; Kis, A. Single-Layer MoS_2 Transistors. *Nat. Nanotechnol.* **2011**, *6*, 147–150.
13. Coleman, J. N.; Lotya, M.; O'Neill, A.; Bergin, S. D.; King, P. J.; Khan, U.; Young, K.; Gaucher, A.; De, S.; Smith, R. J.; *et al.* Two-Dimensional Nanosheets Produced by Liquid Exfoliation of Layered Materials. *Science* **2011**, *331*, 568–571.
14. Xia, F. N.; Mueller, T.; Lin, Y. M.; Valdes-Garcia, A.; Avouris, P. Ultrafast Graphene Photodetector. *Nat. Nanotechnol.* **2009**, *4*, 839–843.
15. Habas, S. E.; Platt, H. A. S.; van Hest, M. F. A. M.; Ginley, D. S. Low-Cost Inorganic Solar Cells: From Ink to Printed Device. *Chem. Rev.* **2010**, *110*, 6571–6594.
16. Antunez, P. D.; Buckley, J. J.; Brutchey, R. L. Tin and Germanium Monochalcogenide IV–VI Semiconductor Nanocrystals for Use in Solar Cells. *Nanoscale* **2011**, *3*, 2399–2411.
17. Xu, Y.; Al-Salim, N.; Bumby, C. W.; Tilley, R. D. Synthesis of SnS Quantum Dots. *J. Am. Chem. Soc.* **2009**, *131*, 15990–15991.
18. Baumgardner, W. J.; Choi, J. J.; Lim, Y.-F.; Hanrath, T. SnSe Nanocrystals: Synthesis, Structure, Optical Properties, and Surface Chemistry. *J. Am. Chem. Soc.* **2010**, *132*, 9519–9521.
19. Zhu, H. L.; Yang, D. R.; Ji, Y. J.; Zhang, H.; Shen, X. F. Two-Dimensional SnS Nanosheets Fabricated by a Novel Hydrothermal Method. *J. Mater. Sci.* **2005**, *40*, 591–595.
20. Koktysh, D. S.; McBride, J. R.; Rosenthal, S. J. Synthesis of SnS Nanocrystals by the Solvothermal Decomposition of a Single Source Precursor. *Nanoscale Res. Lett.* **2007**, *2*, 144–148.
21. Wang, Z. J.; Qu, S. C.; Zeng, X. B.; Liu, J. P.; Zhang, C. S.; Tan, F. R.; Jin, L.; Wang, Z. G. The Application of SnS Nanoparticles to Bulk Heterojunction Solar Cells. *J. Alloys Compd.* **2009**, *482*, 203–207.
22. Franzman, M. A.; Schlenker, C. W.; Thompson, M. E.; Brutchey, R. L. Solution-Phase Synthesis of SnSe Nanocrystals for Use in Solar Cells. *J. Am. Chem. Soc.* **2010**, *132*, 4060–4061.
23. Reddy, N. K.; Devika, M.; Ahsanulhaq, Q.; Gunasekhar, K. R. Growth of Orthorhombic SnS Nanobox Structures on Seeded Substrates. *Cryst. Growth Des.* **2010**, *10*, 4769–4772.
24. Noguchi, H.; Setiyadi, A.; Tanamura, H.; Nagatomo, T.; Omoto, O. Characterization of Vacuum Evaporated Tin Sulfide Film for Solar Cell Materials. *Sol. Energy Mater. Sol. Cells* **1994**, *35*, 325–331.
25. Peter, L. M. Towards Sustainable Photovoltaics: The Search for New Materials. *Philos. Trans. R. Soc., A* **2011**, *369*, 1840–1856.
26. Vaughn, D. D.; In, S. I.; Schaak, R. E. A Precursor-Limited Nanoparticle Coalescence Pathway for Tuning the Thickness of Laterally-Uniform Colloidal Nanosheets: The Case of SnSe. *ACS Nano* **2011**, *5*, 8852–8860.
27. Kang, J. G.; Park, J. G.; Kim, D. W. Superior Rate Capabilities of SnS Nanosheet Electrodes for Li Ion Batteries. *Electrochem. Commun.* **2010**, *12*, 307–310.
28. Ning, J. J.; Xiao, G. J.; Jiang, T.; Wang, L.; Dai, Q. Q.; Zou, B.; Liu, B. B.; Wei, Y. J.; Chen, G.; Zou, G. T. Shape and Size Controlled Synthesis and Properties of Colloidal IV–VI SnSe Nanocrystals. *CrystEngComm* **2011**, *13*, 4161–4166.
29. Zhang, Y.; Lu, J.; Shen, S.; Xu, H.; Wang, Q. Ultralarge Single Crystal SnS Rectangular Nanosheets. *Chem. Commun.* **2011**, *47*, 5226–5228.
30. Greyson, E. C.; Barton, J. E.; Odom, T. W. Tetrahedral Zinc Blende Tin Sulfide Nanoand Microcrystals. *Small* **2006**, *2*, 368–371.
31. Yue, G. H.; Lin, Y. D.; Wen, X.; Wang, L. S.; Chen, Y. Z.; Peng, D. L. Synthesis and Characterization of the SnS Nanowires *via* Chemical Vapor Deposition. *Appl. Phys. A* **2012**, *106*, 87–91.
32. Zhang, H. L.; Hu, C. G.; Wang, X.; Xi, Y.; Li, X. Y. Synthesis and Photosensitivity of SnS Nanobelts. *J. Alloys Compd.* **2012**, *513*, 1–5.
33. Deng, Z. T.; Han, D. R.; Liu, Y. Colloidal Synthesis of Metastable Zinc-Blende IV–VI SnS Nanocrystals with Tunable Sizes. *Nanoscale* **2011**, *3*, 4346–4351.
34. Panda, S. K.; Datta, A.; Dev, A.; Gorai, S.; Chaudhuri, S. Surfactant-Assisted Synthesis of SnS Nanowires Grown on Tin Foils. *Cryst. Growth Des.* **2006**, *6*, 2177–2181.

35. Yue, G. H.; Wang, L. S.; Wang, X.; Chen, Y. Z.; Peng, D. L. Characterization and Optical Properties of the Single Crystalline SnS Nanowire Arrays. *Nanoscale Res. Lett.* **2009**, *4*, 359–363.
36. Nag, A.; Kovalenko, M. V.; Lee, J.-S.; Liu, W.; Spokoyny, B.; Talapin, D. V. Metal-Free Inorganic Ligands for Colloidal Nanocrystals: S^{2-}, HS^-, Se^{2-}, HSe^-, Te^{2-}, HTe^-, TeS_3^{2-}, OH^-, and NH_2^- as Surface Ligands. *J. Am. Chem. Soc.* **2011**, *133*, 10612–10620.
37. Deng, Z. T.; Yan, H.; Liu, Y. Controlled Colloidal Growth of Ultrathin Single-Crystal ZnS Nanowires with a Magic-Size Diameter. *Angew. Chem., Int. Ed.* **2010**, *49*, 8695–8698.
38. Deng, Z.; Mansuripur, M.; Muscat, A. Simple Colloidal Synthesis of Single-Crystal Sb-Se-S Nanotubes with Composition Dependent Band-Gap Energy in the Near-Infrared. *Nano Lett.* **2009**, *9*, 2015–2020.
39. Alivisatos, A. P. Semiconductor Clusters, Nanocrystals, and Quantum Dots. *Science* **1996**, *271*, 933–937.
40. Polking, M. J.; Urban, J. J.; Milliron, D. J.; Zheng, H.; Chan, E.; Caldwell, M. A.; Raoux, S.; Kisielowski, C. F.; Ager, J. W., III; Ramesh, R.; *et al.* Size-Dependent Polar Ordering in Colloidal GeTe Nanocrystals. *Nano Lett.* **2011**, *11*, 1147–1152.
41. Zheng, H.; Rivest, J. B.; Miller, T. A.; Sadtler, B.; Lindenberg, A.; Toney, M. F.; Wang, L.-W.; Kisielowski, C.; Alivisatos, A. P. Observation of Transient Structural-Transformation Dynamics in a Cu_2S Nanorod. *Science* **2011**, *333*, 206–209.
42. Brus, L. Solid State Chemistry - Metastable Dense Semiconductor Phases. *Science* **1997**, *276*, 373–374.
43. Deng, Z. T.; Bao, Z. X.; Cao, L.; Chen, D.; Tang, F. Q.; Wang, F. F.; Liu, C. X.; Zou, B. S.; Muscat, A. J. Spherical Hexagonal Tellurium Nanocrystals: Fabrication and Size-Dependent Structural Phase Transition at High Pressure. *Nanotechnology* **2008**, *19*, 045707.
44. Smith, A. M.; Nie, S. M. Semiconductor Nanocrystals: Structure, Properties, and Band Gap Engineering. *Acc. Chem. Res.* **2010**, *43*, 190–200.
45. Devika, M.; Reddy, N. K.; Patolsky, F.; Gunasekhar, K. R. Ohmic Contacts to SnS Films: Selection and Estimation of Thermal Stability. *J. Appl. Phys.* **2008**, *104*, 124503.
46. Yin, Z. Y.; Li, H.; Jiang, L.; Shi, Y. M.; Sun, Y. H.; Lu, G.; Zhang, Q.; Chen, X. D.; Zhang, H. Single-Layer MoS_2 Phototransistors. *ACS Nano* **2012**, *6*, 74–80.
47. Coropceanu, V.; Cornil, J.; da Silva Filho, D. A.; Olivier, Y.; Silbey, R.; Bredas, J.-L. Charge Transport in Organic Semiconductors. *Chem. Rev.* **2007**, *107*, 926–952.
48. Talapin, D. V.; Lee, J. S.; Kovalenko, M. V.; Shevchenko, E. V. Prospects of Colloidal Nanocrystals for Electronic and Optoelectronic Applications. *Chem. Rev.* **2010**, *110*, 389–458.
49. Fafarman, A. T.; Koh, W. K.; Diroll, B. T.; Kim, D. K.; Ko, D. K.; Oh, S. J.; Ye, X. C.; Doan-Nguyen, V.; Crump, M. R.; Reifsnyder, D. C.; *et al.* Thiocyanate-Capped Nanocrystal Colloids: Vibrational Reporter of Surface Chemistry and Solution-Based Route to Enhanced Coupling in Nanocrystal Solids. *J. Am. Chem. Soc.* **2011**, *133*, 15753–15761.
50. Koh, W. K.; Saudari, S. R.; Fafarman, A. T.; Kagan, C. R.; Murray, C. B. Thiocyanate-Capped PbS Nanocubes: Ambipolar Transport Enables Quantum Dot Based Circuits on a Flexible Substrate. *Nano Lett.* **2011**, *11*, 4764–4767.
51. Fardy, M.; Hochbaum, A. I.; Goldberger, J.; Zhang, M. M.; Yang, P. Synthesis and Thermoelectrical Characterization of Lead Chalcogenide Nanowires. *Adv. Mater.* **2007**, *19*, 3047–3051.
52. Jiang, Y.; Zhang, W. J.; Jie, J. S.; Meng, X. M.; Fan, X.; Lee, S. T. Photoresponse Properties of CdSe Single-Nanoribbon Photodetectors. *Adv. Funct. Mater.* **2007**, *17*, 1795–1800.
53. Sugiyama, M.; Reddy, K. T. R.; Revathi, N.; Shimamoto, Y.; Murata, Y. Band Offset of SnS Solar Cell Structure Measured by X-ray Photoelectron Spectroscopy. *Thin Solid Films* **2011**, *519*, 7429–7431.
54. Vidal, J.; Lany, S.; d'Avezac, M.; Zunger, A.; Zakutayev, A.; Francis, J.; Tate, J. Band-Structure, Optical Properties, and Defect Physics of the Photovoltaic Semiconductor SnS. *Appl. Phys. Lett.* **2012**, *100*, 032104.
55. Johnson, J. B.; Jones, H.; Latham, B. S.; Parker, J. D.; Engelken, R. D.; Barber, C. Optimization of Photoconductivity in Vacuum-Evaporated Tin Sulfide Thin Films. *Semicond. Sci. Technol.* **1999**, *14*, 501–507.
56. Jie, J. S.; Zhang, W. J.; Jiang, Y.; Meng, X. M.; Li, Y. Q.; Lee, S. T. Photoconductive Characteristics of Single-Crystal CdS Nanoribbons. *Nano Lett.* **2006**, *6*, 1887–1892.
57. Konstantatos, G.; Clifford, J.; Levina, L.; Sargent, E. H. Sensitive Solution-Processed Visible-Wavelength Photodetectors. *Nat. Photonics* **2007**, *1*, 531–534.